Air Bubble Collapse in Non-Newtonian Medium with an Application in Biology

Sh. Boland[1], S. Majidi [2], A. Afshari[1*]

[1] School of Mechanical Engineering, College of Engineering, University of Tehran, Tehran, Iran

[2] Faculty of Mechanical and Energy Engineering, Shahid Beheshti University, Tehran, Iran

ABSTRACT: An unsteady compressible multiphase flow solver is developed and used to simulate shock-bubble interaction in a non-Newtonian fluid. A five-equation multiphase model that accounts for capillary and viscous effects is employed and discretized by finite volume methodology. Harten-Lax-Van Leer-contact Riemann solver is invoked to compute the convective fluxes and tangent of hyperbola for interface capturing interface sharpening scheme is applied to reduce the excessive diffusion at the interface. Multiple benchmark problems such as air-helium shock tube, shock cavity interaction, Rayleigh-Taylor instability and underwater explosion are probed to evaluate the performance and accuracy of this method. The results obtained compare well with the available experimental and numerical data. The developed solver is then used to study shock-interface interaction in both Newtonian and non-Newtonian mediums. Non-Newtonian liquid is resembling the blood modeled by Carreau-Yasuda constitutive equation. The obtained results show an expedition of bubble-collapse with a higher jet tip velocity in non-Newtonian medium compared to that in the Newtonian surrounding liquid. Moreover, a third phase adjacent to the bubble collapse is considered and the penetration depth of the re-entrant jet in the neighboring phase is studied as a measure of tissue injury. Our results show that by increasing post shock pressure, the re-entrant jet velocity and thus the penetration depth increases. Furthermore, increasing the adjacent phase viscosity results into less penetration depth in the tissue..

1- Introduction

Cavitation bubbles are believed to play an important role in diverse biomedical applications such as ultrasound-assisted lipoplasty [1,2], brain tumor surgery [3-5], phacoemulsification [6] and shockwave lithotripsy [7-11]. Shockwave lithotripsy is a medical treatment which delivers many positive and negative pressure pulses to the location of kidney stones to break them [12,13]. Passive cavitation is cited as a major physical phenomenon observed in both urine and the surrounding tissues in shockwave lithotripsy procedure [14]. Shockwave propagation within and around stone [15] and cavitation erosion [7,16] due to bubble collapse near stone are two important mechanisms of stone communications. Wang [17] investigated the interaction of kidney stones with the shockwave applied in lithotripsy by using a coupled finite volume-finite element approach. The side effects of shockwave lithotripsy such as tissue damages and vascular injuries have been subject of much interest by biomedical community [14, 18-21]. Shock induced bubble collapse is a vital physical phenomenon embedded in shock-wave lithotripsy procedure. This collapse triggers the emergence of high speed liquid jet impinging the blood vessel and causing tissue damage. Rayleigh [22] was a pioneer to mathematically describe the cavity collapse. The high pressure regions formed in the collapse process are recognized as a major cause of cavitation damage in early researches [23]. Experimental observations have provided an essential understanding of the underlying physics of shock-cavity interaction. Formation of high speed re-entrant jet in the bubble involution phase was first detected by Kornfeld et al. [24] and later witnessed in the experimental study of Benjamin et al. [25] In another remarkable study, Ohl et al. [26] investigated the effect of post-shock pressure variations on the interaction of shock wave with bubbles of various initial radii. The jetting velocity of the liquid phase was observed to increase by increasing the initial bubble radius. Several experimental studies of shock bubble interaction have been conducted using spark discharge method as a practical technique for bubble generation [25, 27-29]. Using this method, Tomita et al. [30] studied bubble collapse near a solid surface achieving a maximum wall pressure of 12 MPa. In addition, Kodama et al. [31] investigated in vivo interaction of a shockwave with gaseous bubble attached to the tissue surface. The tissue surface was resembled by gelatin to which a shockwave with a peak pressure of 10.2 ± 0.5 MPa was applied. The destructive effects of liquid jet caused by collapsing bubble on gelatin surface were experimentally observed. More recently, bubble-sphere interaction near a rigid wall has been captured using high speed imaging technique [32].

Computational fluid dynamics has been proved to be a reliable tool to enhance previous analytical and experimental studies. Several computational methodologies and algorithms were used to simulate bubble collapse near a wall [33-35].

*Corresponding author's email: afsharia@ut.ac.ir

Compressibility of the gas phase was neglected in these numerical studies. Popinet et al. [36] used front-tracking method to examine the impact of viscosity in Rayleigh equation near a wall. However, like potential based methods, their method was not capable of capturing the shock. More recent investigations were performed in fully compressible Eulerian context where shock-interface interaction can be visualized. Ball et al. [37] simulated shock bubble interaction utilizing two-dimensional second-order accurate method. The free-Lagrange computational algorithm is used to simulate the collapse of a cylindrical air cavity in water allows the air/water interface to be tracked throughout the interaction. The gas inside bubble was observed to be heated due to internal reflection of shockwave. One of the most thorough investigations on shock-bubble interaction was performed by Jamaluddin et al. [38] who captured the re-entrant jet penetrating the bubble and the resulting shockwave in the distal side. Rheology of the surrounding liquid phase is believed to play a vital role in the dynamic behavior of the bubble [39-41]. A few numerical studies on bubble collapse in non-Newtonian liquid medium have been conducted in recent years. Among researches in this area, investigations of Walters [42], Lind and Phillips [43] and Rowlatt and Lind [44] can be cited. They considered cavitation in viscoelastic liquid medium using boundary element and spectral element methods. However, shock-interface interaction in a non-Newtonian liquid medium has not been studied. The present study concentrates on interaction of a gaseous bubble with a shockwave propagating in a liquid medium to simulate cavitation bubble collapse in blood flow. Shear-thinning characteristic of the blood is resembled by Carreau-Yasuda constitutive model. Also, the shock wave strength is altered to investigate the effects of post-shock pressure on the re-entrant jet velocity as a major cause of tissue injury in shockwave lithotripsy. Apart from, a 3-phase bubble collapse simulation, the impact of tissue viscosity on penetration depth is studied.

2- Governing Equations and Numerical Scheme

The two-dimensional form of the governing equations for compressible two phase flow without phase change are given below [45]. The three-phase version of the governing equations are presented in Appendix A.

$$U_t + F_x + G_y = S(U) \tag{1}$$

where

$$U = \begin{pmatrix} \rho_1\alpha_1 \\ \rho_2\alpha_2 \\ \rho u \\ \rho v \\ \rho E \end{pmatrix}, F = \begin{pmatrix} \alpha_1\rho_1 u \\ \alpha_2\rho_2 u \\ \rho u^2 + P \\ \rho uv \\ u(\rho E + P) \end{pmatrix}, G = \begin{pmatrix} \alpha_1\rho_1 v \\ \alpha_2\rho_2 v \\ \rho uv \\ \rho v^2 + P \\ v(\rho E + P) \end{pmatrix},$$

$$S = \begin{pmatrix} 0 \\ 0 \\ (\nabla.\tau)_x - \sigma\kappa\dfrac{\partial\alpha_1}{\partial x} + \rho g_x \\ (\nabla.\tau)_y - \sigma\kappa\dfrac{\partial\alpha_1}{\partial y} + \rho g_y \\ \nabla.\left(\vec{u}.\tau\right) - \sigma\kappa(\vec{u}.\nabla\alpha_1) + \rho(\vec{u}.\vec{g}) \end{pmatrix} \tag{2}$$

where $E = e + \dfrac{1}{2}u^2$ and e is specific internal energy. Pressure and specific internal energy are related via stiffened gas equation of state given below [46].

$$P = (\gamma - 1)\rho e - \gamma P_\infty \tag{3}$$

The constitutive equation for generalized Newtonian fluids is defined as

$$\tau = 2\eta(\dot{\gamma})D \tag{4}$$

where D is the strain rate tensor. The constitutive equation of purely viscous non-Newtonian fluid can be expressed by Carreau-Yasuda shear thinning model as [47]

$$\eta(\dot{\gamma}) = \eta_\infty + (\eta_0 - \eta_\infty)[1 + (\lambda\dot{\gamma})^\beta]^{\frac{n-1}{\beta}} \tag{5}$$

where $\dot{\gamma}$ represents shear rate, n indicates power-law index and λ is the relaxation time constant. η_0 corresponds to the zero-shear rate and η_∞ represents the infinite-shear rate which is negligible in practice. The dimensionless parameter β with a practical value of 2 describes the transition region [47]. The reduced equation can be rewritten as follows.

$$\eta(\dot{\gamma}) = \eta_0[1 + (\lambda\dot{\gamma})^2]^{\frac{n-1}{2}} \tag{6}$$

Temporal discretization is carried out utilizing the well-known third-order strong stability preserving Total Variation Diminishing (TVD) Runge-Kutta scheme. The discretized form of the governing equations used in each stage of the Runge-Kutta scheme can be written as below [48].

$$u_i^{n+1} = u_i^n + \frac{\Delta t}{\Delta x}[f_{i-\frac{1}{2}} - f_{i+\frac{1}{2}}] + S_i^n \quad (7)$$

where f is the convective flux and S represents non-convective terms. The convective fluxes are measured based on the procedure used in approximate Harten-Lax-van Leer-Contact (HLLC) Riemann solvers [48]. In this procedure, the highest wave speeds in right and left directions are defined as

$$S_R = \max(u_L + c_L, u_R + c_R)$$
$$S_L = \max(u_L - c_L, u_R - c_R) \quad (8)$$

where c indicates the speed of sound (Eq. (9)) and subscripts R and L represent right and left directions.

$$c = \sqrt{\frac{\gamma(P + P_\infty)}{\rho}} \quad (9)$$

Then, HLLC based convective can be obtained as follows.

$$F_{i+\frac{1}{2}}^{hllc} = \begin{cases} F(U_L) & \text{if} \quad 0 \leq S_L \\ F_{*L} & \text{if} \quad S_L \leq 0 \leq S_* \\ F_{*R} & \text{if} \quad S_* \leq 0 \leq S_R \\ F(U_R) & \text{if} \quad 0 \geq S_R \end{cases} \quad (10)$$

The parameters in the star region, confined between left and right running waves is defined as below

$$F_{*K} = F_K + S_K(U_{*K} - U_K) \quad (11)$$

where U_{*K} is the vector of intermediate state, defined in Eq. (12).

$$U_{*K} = \rho_K (\frac{S_K - u_K}{S_K - S_*}) \begin{pmatrix} 1 \\ S_* \\ E_K + (S_* u_K)[S_* + \frac{P_K}{\rho_K(S_K - u_K)}] \end{pmatrix} \quad (12)$$

In Eq. (12), S_* is the sound speed in the intermediate region, approximated as follows.

$$S_* = \frac{P_R - P_L + \rho_L u_L(S_L - u_L) - \rho_R u_R(S_R - u_R)}{\rho_L(S_L - u_L) - \rho_R(S_R - u_R)} \quad (13)$$

Volume of fluid method [49] is employed to capture interfacial evolutions. Second order Monotonic Upwind Scheme for Conservation Laws (MUSCL) [50] method is used to reconstruct the solution vector including volume fraction and conservative variables in computational cell edges.

In Fig. 1, the flowchart of solution procedure is shown. First, the conservative variables are calculated using Eq. (2). Next, wave speeds and fluxes are computed using Eqs. (8) and (10). Consecutively, conservative variables and volume fraction are updated in the entire domain. Then, the viscous and interfacial source terms are updated using the new values of the conservative variables. At the end of the time step, primary variables are updated based on the new values of the conservative variables.

3- Results

In order to validate the developed numerical algorithm multiple test cases including helium-air one-dimensional shock tube, collapse of gas bubble in liquid medium, underwater explosion, and Rayleigh-Taylor instability are investigated and compared with numerical and experimental data. After validation, shock-bubble interaction in Carreau-Yasuda non-Newtonian fluid with blood rheological characteristic is simulated and compared to Newtonian fluid. In addition, the effects of bubble collapse on the bordering tissue is investigated and the impact of tissue viscosity on penetration depth is examined.

3- 1- Benchmark problems

In this section, the results for benchmark problems are presented and discussed.

3- 1- 1- Air-helium shock tube

As the first benchmark problem, helium-air one-dimensional shock tube, previously investigated by So et al. [51] is used to perform grid sensitivity analysis.

The initial condition of this problem is considered as below:

$$(p, \rho, u, v, \gamma) = \begin{cases} (1, 1, 0, 0, 1.4) & x < 0.5 \\ (0.1, 0.125, 0, 0, 1.667) & x \geq 0.5 \end{cases} \quad (14)$$

The computations are done for four different grids with size of the cell edges sequentially halved. The variation diagrams of pressure and velocity are shown in Fig. 2 along with their analytical counterparts. The numerical results are seen to be in coincidence with the analytical solution. Moreover, calculated error norms are presented in Table 1. Both $L1$ and $L2$ error norms are seen to be reduced linearly by increasing the resolution, and thus convergence of the numerical results to the exact solution is proved.
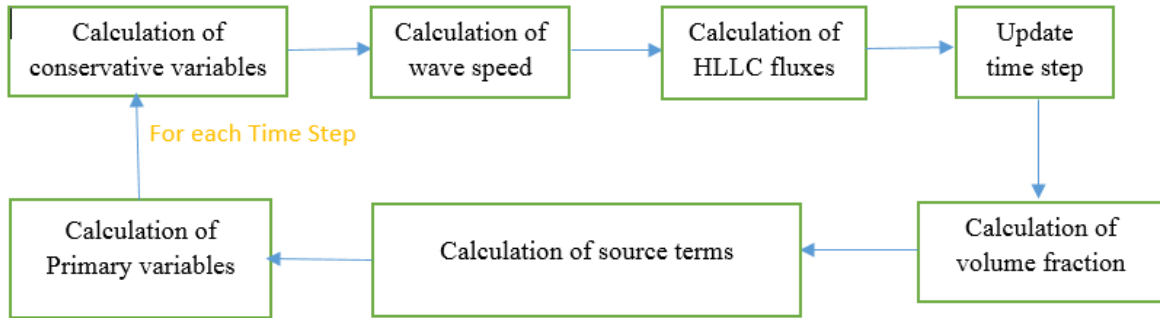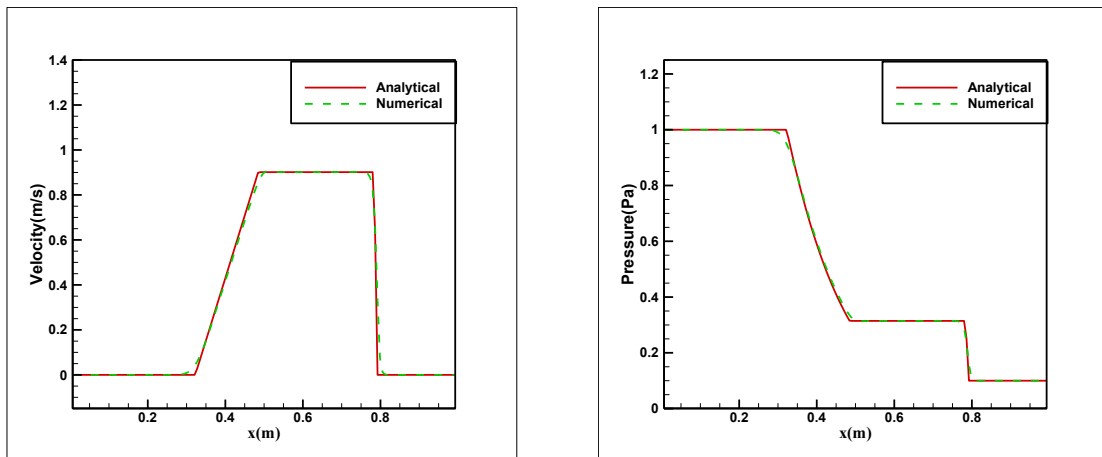
Fig. 1. Flow chart of the solution procedure.

Fig. 2. Air-helium shock tube problem at t=0.15 s, solid lines indicate exact solution while dashed lines indicate the numerical solution.

Table 1. L1 and L2 norm for air-helium shock tube problem.

Mesh resolution	*L1* norm	*L2* norm
200	0.017	0.004
400	0.010	0.002
800	0.005	0.001
1600	0.002	0.0003

3- 1- 2- Gas bubble collapse in water

This benchmark problem is an appropriate test case to evaluate the performance of numerical algorithm in large density variations across the interface. This problem has been investigated both experimentally by Bourne and Field [52] and numerically by Terashima and Tryggvason [53] and Nourgaliev et al. [54]. In this simulation, the cylindrical air bubble of $d = 6$ mm is surrounded by water as a compressible fluid. A square domain of 24×24 mm^2 is covered by 400×400 uniform grid. A shockwave with speed of $u = 681.58 \frac{m}{s}$ located at x=6.6 mm is delivered toward bubble (Fig. 3). Non-reflecting boundary condition is assumed for left and right sides of computational domain while slip wall is imposed on top and bottom. Also the thermodynamic constants are given in the following.

$$(P, \rho, \gamma, P_\infty) = \begin{cases} (10^5, 1.2, 1.4, 0) & \text{Air cavity} \\ (1.9 \times 10^9, 1323.6, 4.1, 8 \times 10^8) & \text{Post-Shock water} \\ (10^5, 1000, 4.1, 8 \times 10^8) & \text{Pre-Shock water} \end{cases} \quad (15)$$

After the incident shock hits the upstream side of the bubble, a shockwave is transmitted into the gaseous phase with lower acoustic impedance and simultaneously a rarefaction wave is reflected into water with higher acoustic impedance (Fig. 4(a)). The difference in sound speeds of water and air leads to the formation of a water penetrating the bubble on its upstream side (Fig. 4(b)). As the time passes, the liquid jet penetrates further into the bubble (Fig. 4(c)), and the bubble splits to two smaller bubbles eventually (Fig. 4(d)). The maximum jet velocity of $2914 \, m/s$ is reached immediately after splitting the bubble, at $t = 3.69 \mu s$. The obtained maximum jet velocity is in good agreement with those reported by Nourgaliev et al. [54] (2850 m/s) and Bo and Grove [55] (2830 m/s).

Aside from the hydrodynamic evolution of the flow field, other interesting physical features have been witnessed in the experimental study of shock-cavity interaction and often not visualized in numerical simulations of this flow field [52]. Among these features is the light flashing a few moments after bubble breakup and formation of lobes. This luminescence is attributed to the abrupt heating the gas trapped inside the bubble due to the passage of the violent compressive shock. After the liquid jets drives through the bubble forming two separate gas pockets, gas temperature inside the pockets reaches a very high level enough to emit light. Typical duration of this so called sonoluminescence is in the order of microseconds in the experimental observations of Bourn and Field [52] for a shock of pressure 1.9 GPa hitting a cavity of diameter 6 mm.

3- 1- 3- Underwater explosion

In order to demonstrate the performance of our numerical algorithm in the presence of shockwave and rarefaction wave, simulation of underwater explosion is carried out. Underwater explosion was performed by Shyue [49] and Bo and Grove [55]. The computational domain is a rectangle of $[0,4] \times [0,3]$ while the interface between water and air is located at $y = 1.5$ m. The initial conditions of both phases are given as:
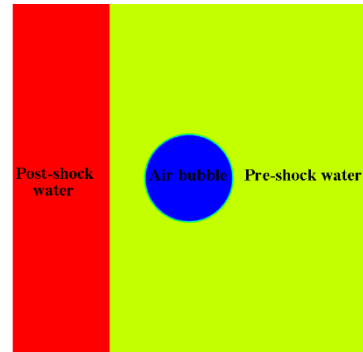

Fig. 3. Initial condition.

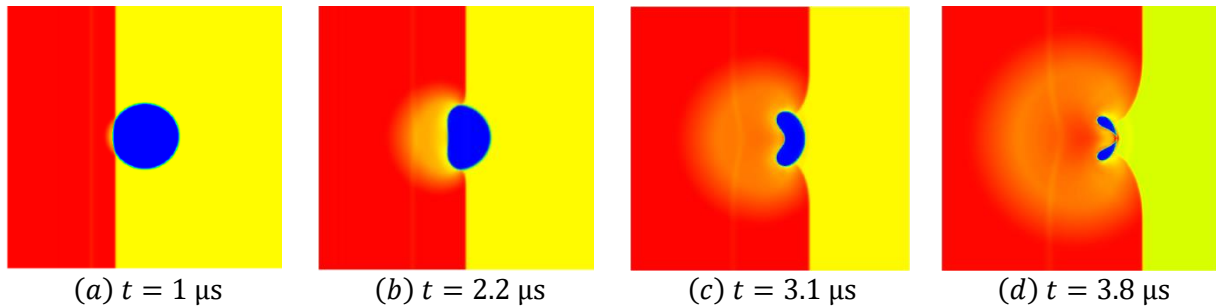(a) $t = 1$ μs   (b) $t = 2.2$ μs   (c) $t = 3.1$ μs   (d) $t = 3.8$ μs

Fig. 4. Density contours in shock induced collapse of air cavity.

$$(P,\rho,\gamma,P_\infty) = \begin{cases} (1.01325\times10^5\,\text{Pa}, 1.225\,\dfrac{\text{kg}}{\text{m}^3}, 1.4, 0) \\ \text{for air} \\ (1.01325\times10^5\,\text{Pa}, 1000\,\dfrac{\text{kg}}{\text{m}^3}, 4.4, 6\times10^8) \\ \text{for water} \end{cases} \quad (16)$$

Initially, gas bubble of diameter $0.24\,\text{m}$, pressure $1\,\text{GPa}$ and density $1250\,\text{kg}/\text{m}^3$ is situated in liquid phase and centered at $(2.1, 1.2)\,\text{m}$. The domain is covered by a uniform grid consisting of 400×300 computational cells. As it is shown in Fig. 5, at the beginning, high pressure in the air bubble leads to formation of a non-stationary shock front with outward direction in the liquid phase and an inward moving rarefaction wave in the compressed gas bubble. Furthermore interaction between outward shock wave and the interface reflects a rarefaction wave. Reflection of this wave results in changing the shape to ellipsoidal bubble and accelerates the bubble upward. As shown in Fig. 6 the results are in good agreement with those presented by shyue [49].

3- 1- 4- Rayleigh-Taylor instability

To evaluate the numerical methodology at the presence of surface tension, gravity and viscous stress Rayleigh-Taylor instability is simulated using the developed compressible multiphase flow solver and the predicted results are compared to those of Terashima and Tryygvason [53]. Computational domain of 1 m length and 4 m width is covered by 50×200 cells. The fluid with density $0.225\,kg/m^3$ is located in the top while the lighter fluid with the density of $0.1694\,kg/m^3$ is located at the bottom. Surface tension, viscosity and gravity are set equal to $0.1531\,N/m$, $0.00313\,Pa.s$ and $9.8\,m/s^2$ respectively. Wall boundary condition is imposed on the top and bottom and periodic boundary condition is assumed on the left and right sides. Moreover the interface is initially perturbed by using of $y = 2 + 0.05\cos(2\pi x)$.

As shown in Figs. 7(a) and 7(b) the heavy fluid falls down and the lighter fluid ascends along the vertical edges. In addition, in the absence of surface tension the famous mushroom shape of surface is formed (Fig. 7(a)). Also the spike position versus time diagram for both with surface tension and without surface is plotted (Fig. 8) and the results are in good agreement with those presented by Terashima and Tryygvason [53].
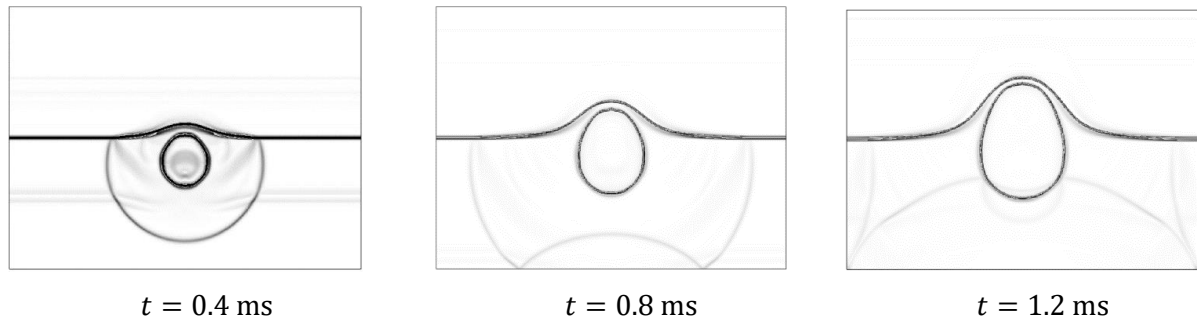

| $t = 0.4$ ms | $t = 0.8$ ms | $t = 1.2$ ms |

Fig. 5. Density schilleren in underwater explosion.

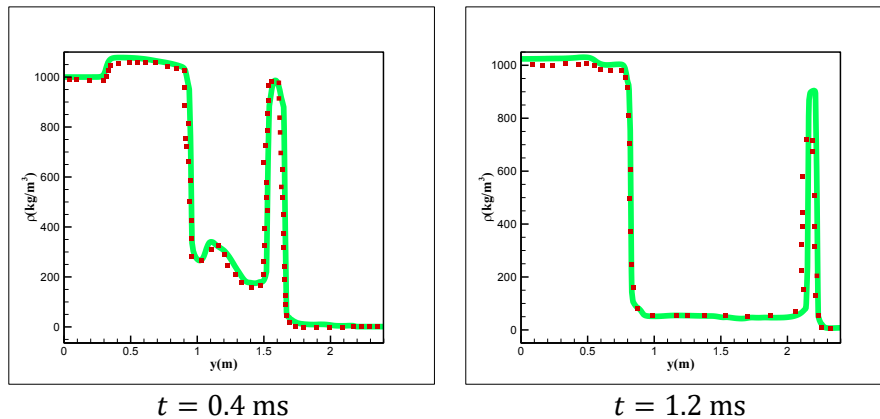

| $t = 0.4$ ms | $t = 1.2$ ms |

Fig. 6. Density distribution along the vertical center-line. The green line indicates the present numerical results and the red symbols represent Shyue [49] results.
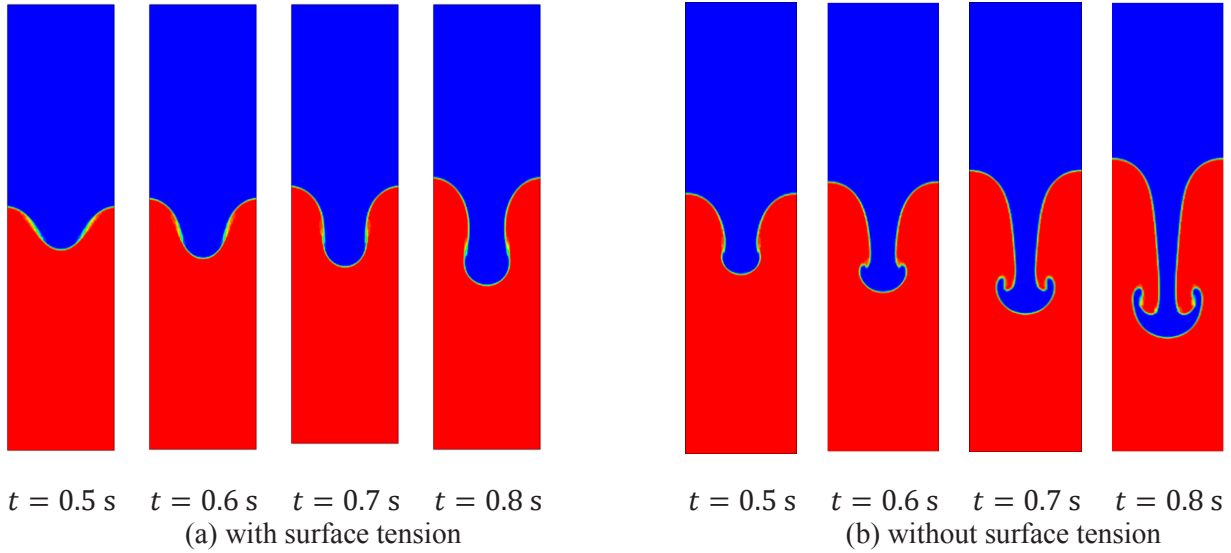
| $t = 0.5\,\text{s}$ | $t = 0.6\,\text{s}$ | $t = 0.7\,\text{s}$ | $t = 0.8\,\text{s}$ |

(a) with surface tension

| $t = 0.5\,\text{s}$ | $t = 0.6\,\text{s}$ | $t = 0.7\,\text{s}$ | $t = 0.8\,\text{s}$ |

(b) without surface tension

Fig. 7. Volume fraction contours in Rayleigh-Taylor instability.

3- 2- Two phase shock bubble interaction

After validating our developed numerical solver through simulating various benchmark problems, two-phase shock-bubble interaction is investigated in the present section. The simulations are performed in a square domain with its edge of size $80\,\mu n$, covered by 100×100 uniform grid. An air bubble of $20\,\mu m$ diameter and atmospheric pressure is situated at $x = 40\,\mu m$ and surrounded by a non-Newtonian fluid with rheological characteristics resembling those of blood (Table 2). It is then compared to bubble collapse in a Newtonian liquid with a viscosity equal to the zero shear rate viscosity (η_0) of the non-Newtonian liquid. A shockwave initially located at $x = 22\,\mu m$, moves toward the bubble with speed of 28.13 m/s (Fig. 9). Right and left boundaries are considered to be non-reflecting, while slip wall boundary condition is imposed on bottom and top edges.

Initial conditions are given as follows.

Fig. 8. Spike position versus time.

$$(P,\rho) = \begin{cases} (1\text{atm}, 1.2\,\dfrac{\text{kg}}{\text{m}^3}) & \text{Air cavity} \\[2mm] (80\text{MPa}, 1000\,\dfrac{\text{kg}}{\text{m}^3}) & \text{Post-Shock blood} \\[2mm] (1\text{atm}, 1000\,\dfrac{\text{kg}}{\text{m}^3}) & \text{Pre-Shock blood} \end{cases} \quad (17)$$

Due to the difference in the acoustic impedance of gas and liquid phase, a liquid jet is formed near the upstream side of the bubble after incident shockwave hits the bubble. This re-entran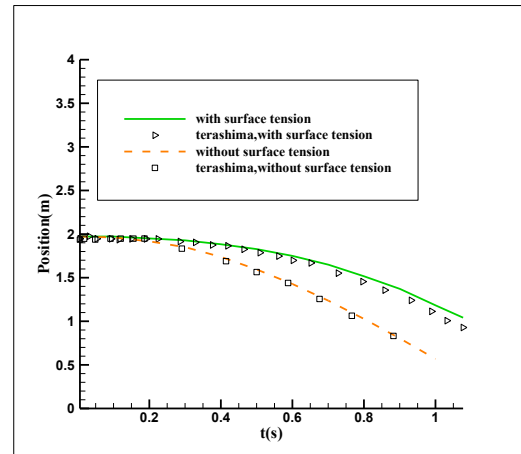t jet drives through the bubble causing involution and eventual collapse of the bubble. Bubble collapse occurring in Newtonian and shear-thinning media are shown in Figs. 10 and 11.

Velocity distribution along the domain centerline is demonstrated in Fig. 12 as a measure of jet formation and propagation in both Newtonian and non-Newtonian cases. As expected, upstream jet speed is higher in non-Newtonian case relative to its Newtonian counterpart due to existence of the shear-thinning property. Consequently, bubble collapse occurs earlier in the non-Newtonian medium (Fig. 13) causing an expedition in formation of re-entrant jet.

Because of the shear thinning characteristic of non-Newtonian fluid, viscosity decreases with increasing shear rate. Therefore the jet velocity is expected to increase with lowering viscosity. The re-entrant jet velocity in

non-Newtonian fluid is obtained 339.313 m/s (Fig. 11) at $t=0.077\mu s$ (Fig. 12) while the re-entrant jet velocity in Newtonian fluid is 138.592 m/s at $t = 0.1\mu s$ (Fig. 12). Consequently, the sharp difference between re-entrant jet velocity in Newtonian versus non-Newtonian fluid indicates the importance of shear thinning characteristic of blood in shockwave lithotripsy under the given operating condition.

When it comes to shockwave strength it is worthwhile to mention that in shockwave lithotripsy treatment of kidney stone, lithotripter can produce pressure pulses with the peak positive pressure between 30 MPa and 110 MPa. Numerical simulations are carried out for several shock strength in this range as presented in Table 3. Increasing shock strength has profound impact on re-entrant jet velocity as depicted in Fig. 14.

The most side effect likely to occur in shockwave lithotripsy is the damage caused by the re-entrant jet formed during bubble collapse and the consequent hemorrhage. Thus, the importance of re-entrant jet velocity in hemorrhage reduction should be perceived. Unfortunately, in most of the numerical simulations the effect of Non-Newtonian stress on re-entrant jet velocity was neglected and shock bubble interaction was simulated in a Newtonian fluid while in present study the intense influence of shear thinning behavior of blood versus Newtonian is discussed. The re-entrant jet velocity in blood for post pressure of 80 MPa is almost 70 m/s more than re-entrant jet velocity in Newtonian fluid with similar zero shear

rate. Thus, taking into account the shear-thinning property of the blood flow is an important step to achieve a more realistic simulation of the complicated physics underlying the shockwave lithotripsy procedure.

3- 3- Three phase shock bubble interaction

In this section, the computational domain includes a third phase representing vessel tissue. A square domain of length $120\mu m$ is covered by a uniform grid with 200×200 cells. The air bubble of $20\mu m$ diameter is located at $(40.60)\mu m$. A shockwave form $x = 22\mu m$ with post shock pressure of 80 MPa which is in the range of the peak positive pressures produced by conventional lithotripters. The shockwave propagation speed is $28.13\ \text{m}/\text{s}$ (Fig. 15). Top and bottom boundaries are assumed to be slip walls while non-reflecting boundary conditions are imposed on left and right edges. The initial condition is given as:

$$(P,\rho) = \begin{cases} (1\text{atm}, 1.2\frac{\text{kg}}{\text{m}^3}) & \text{Air cavity} \\ (80\text{MPa}, 1000\frac{\text{kg}}{\text{m}^3}) & \text{Post-Shock blood} \\ (1\text{atm}, 1000\frac{\text{kg}}{\text{m}^3}) & \text{Pre-Shock blood} \quad (18) \\ (1\text{atm}, 1000\frac{\text{kg}}{\text{m}^3}) & \text{Pre-shock bordering tissue} \end{cases}$$

Here, predicted results of bubble collapse near a stationary medium with a viscosity of 0.01 Pa.s, representing the tissue constituting the blood vessel, are presented. Re-entrant jet penetration is a main cause of tissue damage in shockwave lithotripsy [18,19]. In Fig. 16, the collapse procedure and subsequent re-entrant jet penetrating the tissue are demonstrated.

The forming re-entrant jet affects both the tissue and existing kidney stones. Spark generated in the first focal point of lithotripter causes the formation of shockwave which are then conducted to the second focal point. This focal point is set to be situated at the location of kidney stones. In the last part of our study, tissue viscosity is altered in a range of 0.001 Pa.s to 1 Pa.s to investigate the effect of tissue viscosity on penetration depth of the re-entrant jet. In Fig. 17, penetration depths of re-entrant liquid jets at various tissue viscosities

Fig. 9. The schematic of 2-phase shock bubble interaction.

Table 2. Rheological characteristic of blood as a Carreau-Yasuda model [56].

Zero shear rate limit (η_0)	0.046 Pa. s
Infinite shear rate limit (η_∞)	0.0035 Pa. s
Power low index in Carreau-Yasuda model (n)	0.3568
Relaxation time constant (λ)	3.313 s

| $t = 0.05$ µs | $t = 0.069$ µs | $t = 0.073$ µs | $t = 0.1$ µs (collapse time) |
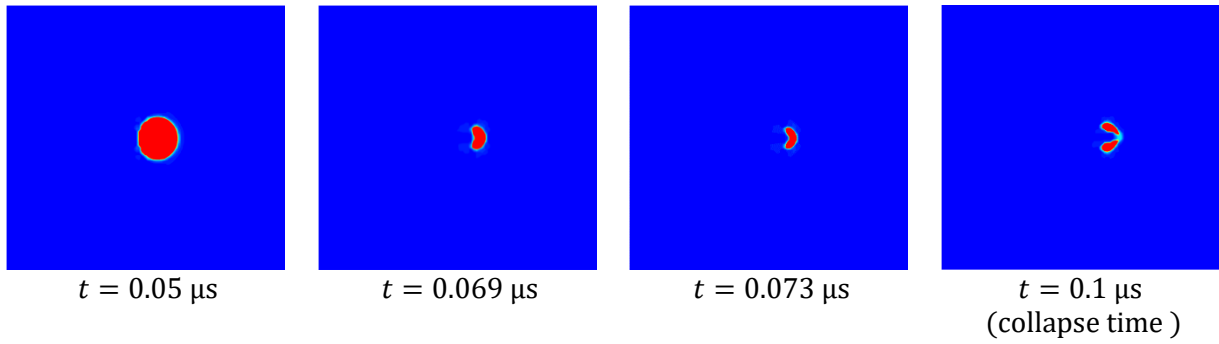
Fig. 10. Volume fraction for bubble collapse in Newtonian fluid.

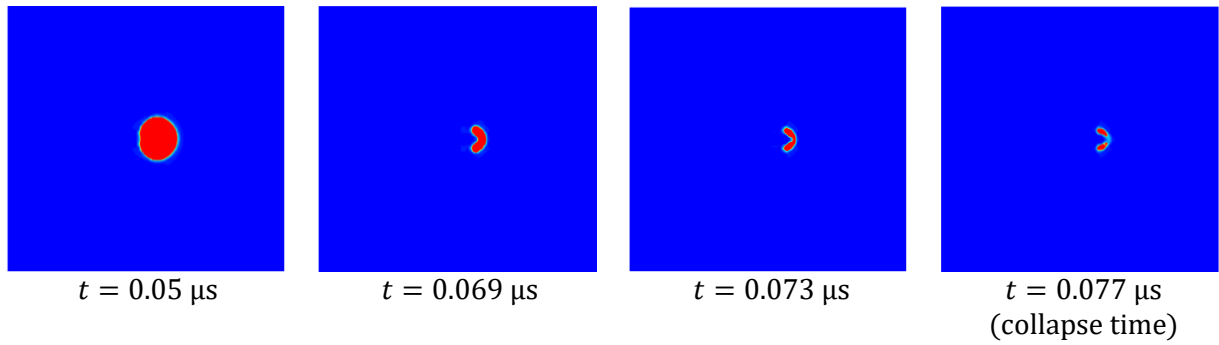| $t = 0.05$ µs | $t = 0.069$ µs | $t = 0.073$ µs | $t = 0.077$ µs (collapse time) |

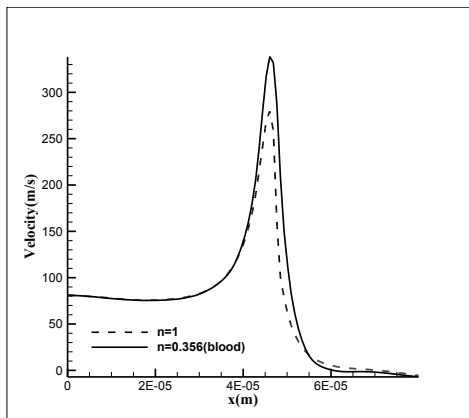**Fig. 11. Volume fraction for bubble collapse in non-Newtonian fluid.**

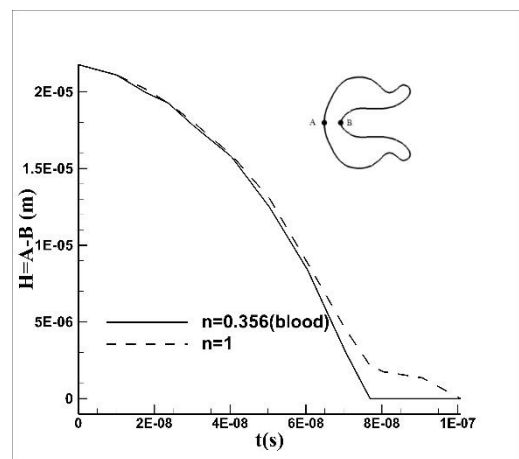**Fig. 12. Velocity profile in domain centerline at t=0.077 µs for Newtonian and non-Newtonian fluid.**

Fig. 13. Bubble deformation versus time measured by the variation of the distance H between upstream side B and downstream side of the interface A.
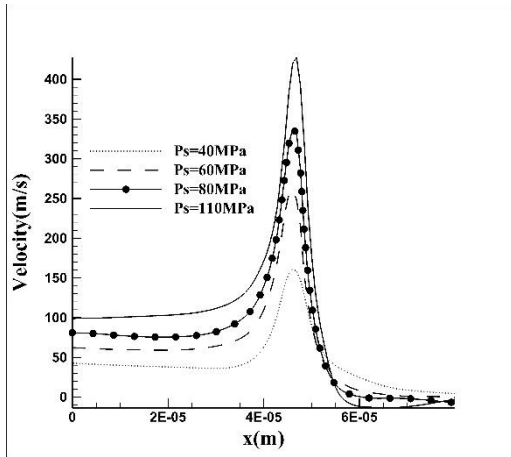
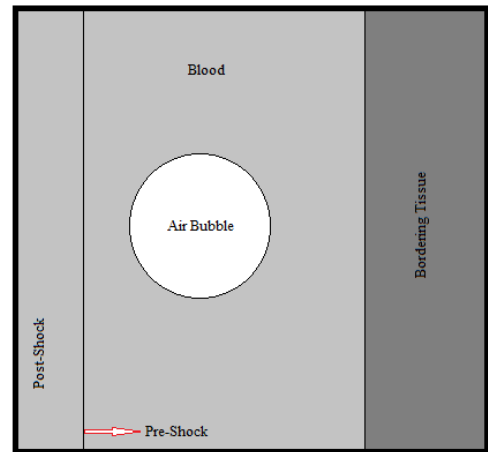**Fig. 14. Velocity diagram in the center of domain at collapse time.**

Fig. 15. The schematic of 3-phase shock bubble interaction.

Table 3. Shockwave speed in different shockwave strength.

Post shock pressure	Shock wave strength
Ps=40 MPa	*Ma*=1.30
Ps=60 MPa	*Ma*=1.55
Ps=80 MPa	*Ma*=1.75
Ps=110 MPa	*Ma*=1.97

$t = 0$ $t = 0.033\ \mu s$ $t = 0.096\ \mu s$

$t = 0.18\ \mu s$ $t = 0.36\ \mu s$ $t = 0.58\ \mu s$
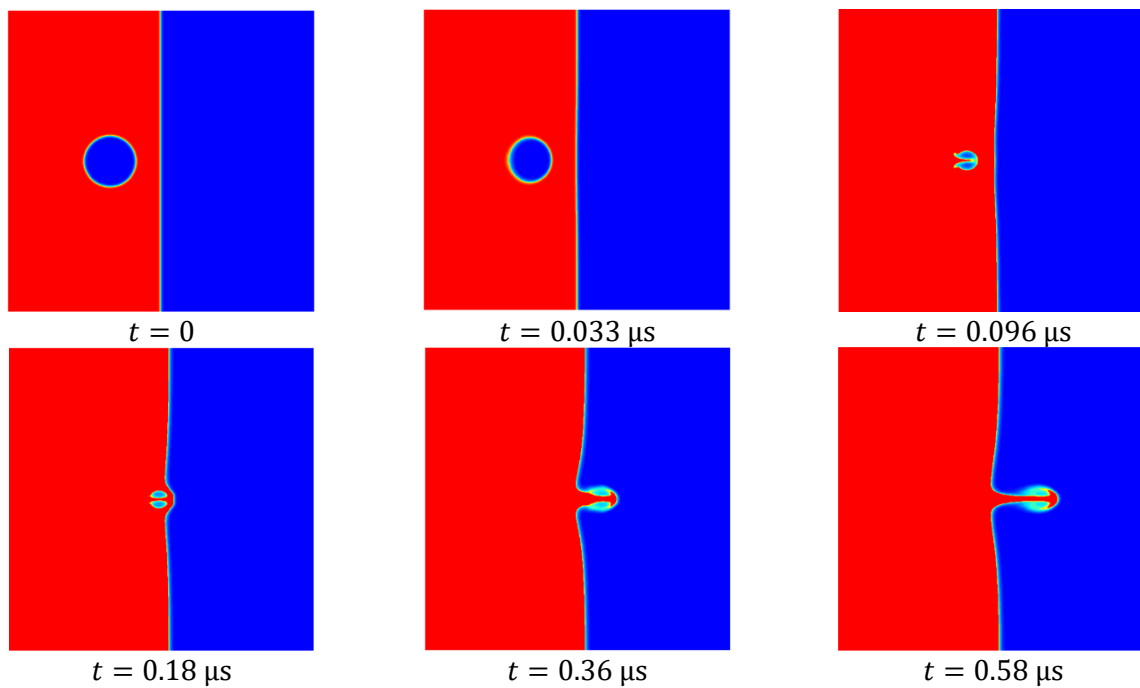
Fig. 16. Volume fraction in different time.

$$\mu = 0.001 \, \text{Pa.s} \qquad \mu = 0.01 \, \text{Pa.s} \qquad \mu = 0.1 \, \text{Pa.s} \qquad \mu = 1 \, \text{Pa.s}$$

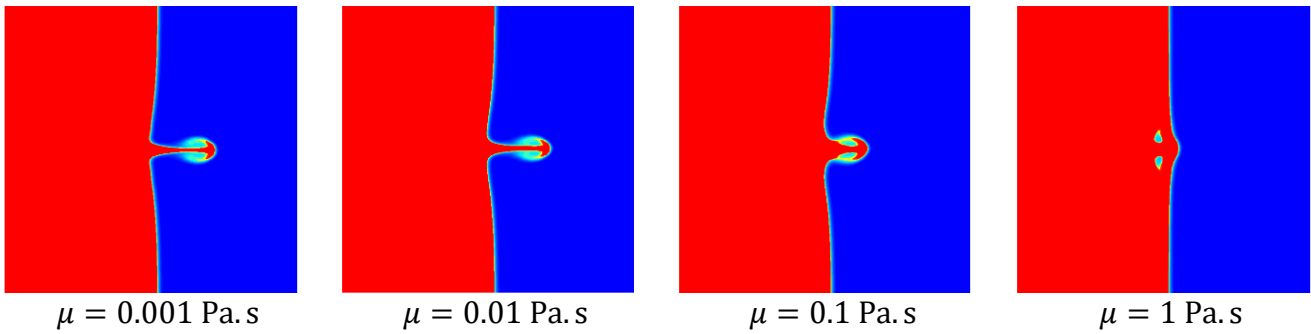**Fig. 17. Volume fraction in different viscosity and the effect of viscosity on penetration depth at t=0.58 μs.**
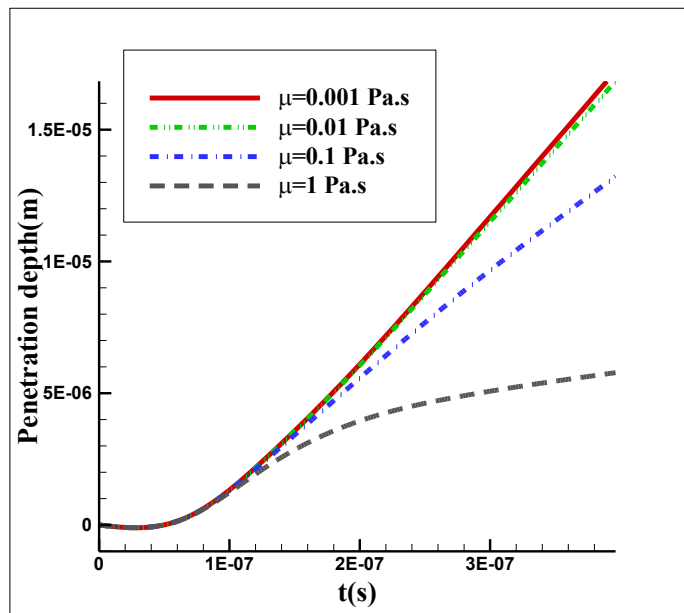

Fig. 18. Penetration depth versus time in different bordering tissue viscosity.

are presented. It is seen that increasing the tissue viscosity leads to lower penetration lengths. In Fig. 18, variation of penetration depths versus time for different tissue viscosities are quantitatively compared.

4- Conclusion

A compressible multiphase flow algorithm was developed and evaluated by multiple benchmark problems such as shock bubble interaction, underwater explosion and Rayleigh-Taylor instability. The performance of computational code in the presence of surface tension, gravity, shockwave and viscous stresses was examined and compared well with available numerical and experimental data. The flow solver then was used to study shock-bubble interaction in non-Newtonian medium. Our results indicated that the bubble collapse occurs sooner in the shear thinning liquid. Additionally, the propagation speed of re-entrant jet was shown to be considerably higher compared to its Newtonian counterpart pronouncing the importance of modeling the non-Newtonian behavior of the blood flow. Finally, the computational domain was extended to include the adjacent tissue and it was concluded that the penetration depth decreases by increasing the tissue viscosity.

Nomenclature

ρ	Density
P	Thermodynamic pressure
u, v	Velocity components in Cartesian coordinates
E	Specific total energy
e	Specific internal energy
α	Volume fraction
γ, P_∞	Thermodynamic constants
c	Sound speed
U	Vectors of conservative variables
F, G	Vectors of fluxes
S	Vectors of source terms

References

[1] R. Cooter, W. Babidge, K. Mutimer, Ultrasound-assisted lipoplasty, ANZ Journal of Surgery, 71(5) (2001) 309-317.

[2] D. Duscher, Z.N. Maan, A. Luan, M.M. Aitzetmüller, E.A. Brett, D. Atashroo, A.J. Whittam, M.S. Hu, G.G. Walmsley, H.-g. Machens, G.C. Gurtner, M.T. Longaker, D.C. Wan, Ultrasound-assisted liposuction provides a source for functional adipose-derived stromal cells, Cytotherapy, 19(12) (2017) 1491-1500.

[3] M. Brock, I. Ingwersen, W. Roggendorf, Ultrasonic aspiration in neurosurgery, Neurosurg Rev, 7(2-3) (1984) 173-177.

[4] T. Sun, Y. Zhang, C. Power, P.M. Alexander, J.T. Sutton, M. Aryal, Closed-loop control of targeted ultrasound drug delivery across the blood – brain / tumor barriers in a rat glioma model, Proceedings of the National Academy of Sciences of the United States of America, 114(48) (2017) E10281-E10290.

[5] Y.-T. Wu, A. Adnan, Effect of Shock-Induced Cavitation Bubble Collapse on the damage in the Simulated Perineuronal Net of the Brain, Scientific Reports, 7(1) (2017) 5323.

[6] H.B. Dick, T. Schultz, A Review of Laser-Assisted Versus Traditional Phacoemulsification Cataract Surgery, Ophthalmology and Therapy, 6(1) (2017) 7-18.

[7] A.J. Coleman, J.E. Saunders, L.A. Crum, Acoustic cavitation generated by an extracorporeal shockwave lithotripter, Ultrasound Med. Biol, 13(2) (1987) 69-76.

[8] S. Cao, Y. Zhang, Assessing the effect of lithotripter focal width on the fracture potential of stones in shockwave lithotripsy, Journal of the Acoustical Society of America, 141(5) (2017) 3718.

[9] M. Shim, M. Park, H.K. Park, The efficacy of performing shockwave lithotripsy before retrograde intrarenal surgery in the treatment of multiple or large (≥1.5 cm) nephrolithiasis: A propensity score matched analysis, investigative and clinical urology, 58(1) (2017) 27-33.

[10] C.K. Turangan, G.J. Ball, A.R. Jamaluddin, T.G. Leighton, Numerical studies of cavitation erosion on an elastic – plastic material caused by shock-induced bubble collapse Subject Areas, Proceedings of the Royal Society A: Mathematical, Physical and Engineering Sciences, 473(2205) (2017) 20170315.

[11] D. Igra, O. Igra, Numerical investigation of the interaction between a planar shock wave with square and triangular bubbles containing different gases, Physics of Fluids, 30(5) (2018) 056104.

[12] R.O. Cleveland, M.R. Bailey, N. Fineberg, Design and characterization of a research electrohydraulic lithotripter patterned after the Dornier HM3, Rev. Sci. Instrum., 71(6) (2000) 2514-2525.

[13] V. Coralic, T. Colonius, Shock-induced collapse of a bubble inside a deformable vessel, Eur J Mech B Fluids, 40 (2013) 64-74.

[14] M.R. Bailey, Y.A. Pishchalnikov, Cavitation detection during shock-wave lithotripsy, Ultrasound Med. Biol., 31(9) (2005) 1245-1256.

[15] M. Lokhandwalla, B. Sturtevant, Fracture mechanics model of stone comminution in ESWL and implications for tissue damage, Phys. Med. Biol, 45(7) (2000) 1923-1940.

[16] L.A. Crum, Cavitation microjets as a contributory mechanism for renal calculi disintegration in ESWL, J. Urol., 140(6) (1988) 1587-1590.

[17] K.G. Wang, Multiphase Fluid-Solid Coupled Analysis of Shock-Bubble-Stone Interaction in Shockwave Lithotripsy, International Journal for Numerical Methods in Biomedical Engineering, 33(10) (2017) cnm.2855.

[18] H. Chen, A. Brayman, M.R. Bailey, Blood vessel rupture by cavitation, Urol. Res, 38(4) (2010) 321-326.

[19] H. Chen, W. Kreider, A.A. Brayman, M.R. Bailey, T.J. Matula, Blood vessel deformations on microsecond time scales by ultrasonic cavitation, Physical Review Letters, 106(3) (2011) 034301.

[20] C. Weber, M.E. Moran, E.J. Braun, Injury of rat renal vessels following extracorporeal shock wave treatment, J. Urology,, 147(2) (1992) 476-481.

[21] P. Zhang, Y.F. Zhu, S.L. Zhu, Dynamics of bubble oscillation in constrained media and mechanisms of vessel rupture in SWL., Ultrasound Med. Biol., 27(1) (2001) 119-134.

[22] Rayleigh, On the pressure developed in a liquid during the collapse of a spherical cavity, Phil. Mag., 34(200) (1917) 94-98.

[23] R. Hickling, M.S. Plesset, Collapse and rebound of a spherical bubble in water, Physics of Fluids, 7(1) (1964) 7-14.

[24] M. Kornfeld, L. Suvorov, On the destructive action of cavitation, Journal of Applied Physics, 15(6) (1944) 495-506.

[25] T.B. Benjamin, A.T. Ellis, The Collapse of Cavitation Bubbles and the Pressures thereby Produced against

Solid Boundaries, Philosophical Transactions of the Royal Society of London A: Mathematical, Physical and Engineering Sciences, 260(1110) (1966) 221-240.

[26] C.D. Ohl, R. Ikink, Shock-Wave-Induced Jetting of Micron-Size Bubbles, Physical Review Letters, 90(21) (2003) 214502.

[27] C.L. Kling, F.G. Hammitt, A Photographic Study of Spark-Induced Cavitation Bubble Collapse, J. Basic Eng, 94(4) (1972) 825-832.

[28] B.H.T. Goh, Y.D.A. Oh, E. Klaseboer, S.W. Ohl, B.C. Khoo, A low-voltage spark-discharge method for generation of consistent oscillating bubbles., Review of Scientific Instruments, 84(1) (2013) 014705.

[29] J.A. Cook, A.M. Gleeson, R.M. Roberts, R.L. Rogers, A spark-generated bubble model with semi-empirical mass transport, J. Acoust. Soc. Am., 101(4) (1997) 1908-1920.

[30] Y. Tomita, A. Shima, Mechanisms of impulsive pressure generation and damage pit formation by bubble collapse, J. Fluid Mech, 169 (1986) 535–564.

[31] T. Kodama, K.A.T. Takayama, Dynamic behavior of bubbles during extracorporeal shock-wave lithotripsy, Ultrasound in Medicine and Biology, 24(5) (1998) 723-738.

[32] S. Li, A.M. Zhang, R. Han, Y.Q. Liu, Experimental and numerical study on bubble-sphere interaction near a rigid wall Experimental and numerical study on bubble-sphere interaction near a rigid wall, Physics of Fluids, 29(9) (2017) 092102.

[33] M.S. Plesset, R.B. Chapman, Collapse of an initially spherical vapour cavity in the neighbourhood of a solid boundary, J. Fluid Mech, 47(2) (1971) 283–290.

[34] J.R. Blake, B.B. Taib, G. Doherty, Transient cavities near boundaries. Part 1. Rigid boundary., J. Fluid Mech, 170 (1986) 479–497.

[35] E. Klaseboer, C. Turangan, S.W. Fong, T.G. Liu, Simulations of pressure pulse-bubble interaction using boundary element method, Comput. Methods Appl. Mech. Engrg, 195 (2006) 4287–4302.

[36] S. Popinet, S. Zaleski, Bubble collapse near a solid boundary: a numerical study of the influence of viscosity, Journal of Fluid Mechanics, 464 (2002) 137-163.

[37] G.J.J. Ball, B.P.P. Howell, T.G.G. Leighton, M.J.J. Schofield, Shock-induced collapse of a cylindrical air cavity in water: a Free-Lagrange simulation, Shock Waves, 10(4) (2000) 265-276.

[38] A.R. Jamaluddin, Free-lagrange simulations of shock-bubble interaction in extracorporeal shock wave lithotripsy, University of Southampton, 2005.

[39] S.k. Hara, Dynamics of nonspherical bubbles surrounded by viscoelastic fluid, Journal of Non -Newtonian Fluid Mechanics, 14 (1984) 249-264.

[40] C. Kim, Collapse of spherical bubbles in Maxwell fluids, Journal of Non-Newtonian fluid Mechanic, 55(1) (1994) 37-58.

[41] E.A. Brujan, Y. Matsumoto, T. Ikeda, Dynamics of ultrasound-induced cavitation bubbles in non-Newtonian liquids and near a rigid boundary, Physics of Fluids,

16(7) (2004) 2402.

[42] M.J. Walters, An Investigation into the Effects of Viscoelasticity on Cavitation Bubble Dynamics with Applications to Biomedicine, school of Mathematics Cardiff University, 2015.

[43] [43] S.J. Lind, T.N. Phillips, The influence of viscoelasticity on the collapse of cavitation bubbles near a rigid boundary, Theoretical and Computational Fluid Dynamics, 26(1-4) (2012) 245–277.

[44] C. F.Rowlatt, S. J.Lind, Bubble collapse near a fluid-fluid interface using the spectral element marker particle method with applications in bioengineering, International Journal of Multiphase Flow, 90 (2017) 118-143.

[45] A. Murrone, H. Guillard, A five equation reduced model for compressible two phase flow problems, Journal of Computational Physics, 202(2) (2005) 664-698.

[46] F.H. Harlow, A.A. Amsden, Fluid dynamics: A LASL monograph(Mathematical solutions for problems in fluid dynamics).

[47] L. Zhang, C. Yang, Z.S. Mao, Numerical simulation of a bubble rising in shear-thinning fluids, Journal of Non-Newtonian Fluid Mechanics, 165(11-12) (2010) 555-567.

[48] F. Toro, Riemann solvers and numerical methods for fluid dynamics, a practical introduction,Springer Science & Business Media, 2009.

[49] K.-M. Shyue, An Efficient Shock-Capturing Algorithm for Compressible Multicomponent Problems, Journal of Computational Physics, 142(1) (1998) 208-242.

[50] B. van Leer, Towards the ultimate conservative difference scheme. V. A second-order sequel to Godunov's method, Journal of Computational Physics, 32(1) (1979) 101-136.

[51] K. So, X. Hu, N. Adams, Anti-Diffusion Interface Sharpening Technique for Two Phase Compressible Flow Simulations, J. Comput. Phys., 231(11) (2012) 4304-4323.

[52] N.K. Bourne, J.E. Field, Shock-induced collapse of single cavities in liquids, Journal of Fluid Mechanics, 244 (1992) 225-240.

[53] H. Terashima, G. Tryggvason, A front-tracking/ghost-fluid method for fluid interfaces in compressible flows, Journal of Computational Physics, 228(11) (2009) 4012-4037.

[54] R.R. Nourgaliev, T.N. Dinh, T.G. Theofanous, Adaptive characteristics-based matching for compressible multifluid dynamics, Journal of Computational Physics, 213(2) (2006) 500-529.

[55] W. Bo, J.w. Grove, A volume of fluid method based ghost fluid method for compressible multi-fluid flows, Computers and Fluids, 90 (2014) 113-122.

[56] S.S. Shibeshi, W.E. Collins, The Rheology of Blood Flow in a Branched Arterial System, Appl Rheol, 15(6) (2005) 398-405.

Appendix A:

The governing two dimensional equations for compressible three phase flow without phase change are:

$$U_t + F_x + G_y = S(U) \tag{A1}$$

$$U = \begin{pmatrix} \rho_1\alpha_1 \\ \rho_2\alpha_2 \\ \rho_3\alpha_3 \\ \rho u \\ \rho v \\ \rho E \end{pmatrix}, F = \begin{pmatrix} \alpha_1\rho_1 u \\ \alpha_2\rho_2 u \\ \alpha_3\rho_3 u \\ \rho u^2 + P \\ \rho uv \\ u(\rho E + P) \end{pmatrix}, G = \begin{pmatrix} \alpha_1\rho_1 v \\ \alpha_2\rho_2 v \\ \alpha_3\rho_3 v \\ \rho uv \\ \rho v^2 + P \\ v(\rho E + P) \end{pmatrix},$$

$$\tag{A2}$$

$$S = \begin{pmatrix} 0 \\ 0 \\ 0 \\ (\nabla.\tau)_x - \sigma\kappa\dfrac{\partial\alpha_1}{\partial x} + \rho g_x \\ (\nabla.\tau)_y - \sigma\kappa\dfrac{\partial\alpha_1}{\partial y} + \rho g_y \\ \nabla.\left(\vec{u}.\tau\right) - \sigma\kappa(\vec{u}.\nabla\alpha_1) + \rho(\vec{u}.\vec{g}) \end{pmatrix}$$

The mixture variables for three phase flow can be defined as follow:

$$\alpha_1 + \alpha_2 + \alpha_3 = 1 \tag{A3}$$

$$\rho = \alpha_1\rho_1 + \alpha_2\rho_2 + \alpha_3\rho_3 \tag{A4}$$

$$\rho E = \alpha_1\rho_1 E_1 + \alpha_2\rho_2 E_2 + \alpha_3\rho_3 E_3 \tag{A5}$$